



False Planets around Giant Stars: A Case Study of Sanders 364 in M67

Qijia Zhou¹ , David W. Latham¹ , Samuel N. Quinn¹ , Allyson Bieryla¹ , Andrew Vanderburg² , Perry Berlind¹,
Michael L. Calkins¹ , and Gilbert A. Esquerdo¹

¹ Center for Astrophysics | Harvard & Smithsonian, 60 Garden Street, Cambridge, MA 02138, USA; qijia.zhou@cfa.harvard.edu

² Department of Physics and Kavli Institute for Astrophysics and Space Research, Massachusetts Institute of Technology, Cambridge, MA 02139, USA
Received 2023 March 10; revised 2023 August 10; accepted 2023 August 16; published 2023 September 18

Abstract

Discovering planets in sparsely populated regions of parameter space is crucial to improving our understanding of planetary formation and evolution. One such region is the subset of planets that orbit giant, evolved stars. However, some of these evolved stars are known to exhibit long-period quasiperiodic radial velocity signals, which can masquerade as signals from orbital motion due to planetary companions. In this paper, we investigate the case of Sanders 364, a K giant star in the old open cluster M67. A paper by Brucalassi et al. reports the discovery of a giant planet with a period of 121 days orbiting Sanders 364. From our analysis of a large set of independent radial velocities, we find no convincing evidence for the giant planet reported by Brucalassi et al. We did identify six long-period radial velocity signals of unclear origin, including the 121 days signal reported by Brucalassi et al., but based on our analysis, we speculate that these are quasiperiodic signals that arise from nonplanetary origins, such as stellar variability or aliasing. The results from our study of Sanders 364 suggest that the detection of true orbital motion from a long-period planetary companion requires extra care when the host star is highly evolved. We conclude by offering recommendations for future study of planetary companions around evolved host stars.

Unified Astronomy Thesaurus concepts: [K giant stars \(877\)](#); [Exoplanets \(498\)](#); [Radial velocity \(1332\)](#)

1. Introduction

The business of exoplanet detection is booming—at the time of writing, there have been over 5,000 confirmed planet detections (NASA Exoplanet Science Institute 2020). One interesting population is the subset of planets that orbit giant, evolved stars on their first ascent of the red giant branch. These discoveries illuminate how planetary systems evolve after the star departs the main sequence. The current project will focus on a subset of this population: planets orbiting evolved K giant stars.

Thus far, there have been 72 confirmed planets orbiting evolved K giant stars, mostly discovered using the radial velocity (RV) method (NASA Exoplanet Science Institute 2020). However, K giants are known to exhibit long-term quasiperiodic RV signals with cycles on the order of hundreds of days, which are speculated to have nonplanetary origins (Walker et al. 1989; Hatzes & Cochran 1993; Hatzes et al. 2018; Döllinger & Hartmann 2021). These signals are difficult to disentangle from signals originating from true orbital motion. As a result, many have masqueraded as planets, some of which were later refuted. For example, the discovery of a 629 days planet orbiting Aldebaran (Hatzes et al. 2015) was refuted by Reichert et al. (2019) after introducing additional observations that revealed that the RV variations of Aldebaran are quasiperiodic and not characteristic of orbital motion. In Hatzes et al. (2018), the authors describe that they initially identified coherent, long-lived 702 days RV variations for γ Dra, but additional observations revealed changes in the apparent period and phase of the signal, a clear sign of quasiperiodicity.

In order for discoveries of long-period planets around evolved giant stars to withstand further investigation, authors need to demonstrate satisfaction of three criteria: (1) the periodic signals

are long-lived and coherent (preferably with observations from multiple instruments), (2) the periodic signals are not correlated with activity indicators, and (3) the significance of the peak in the power spectrum improves as more observations are accumulated. Using these conditions as a guideline, this paper presents an independent set of RV observations to test one of the planet discoveries from Brucalassi et al. (2017), hereafter B17: a giant planet orbiting Sanders 364 in M67. Our paper is structured as follows: In Section 2, we describe the host star and the reported planet. In Section 3, we describe our data set. In Section 4, we detail our search for B17's planet using Lomb–Scargle periodograms and the subsequent analysis of the discovered signals. We find no convincing evidence for a strict periodicity at B17's reported period and thus are unable to confirm the existence of the planetary companion. In Section 5, we discuss the five longer period peaks revealed in our analysis to be more significant than the peak reported by B17. We investigate whether these signals could be evidence of planetary companions or another example of nonplanetary RV variations masquerading as planets. In Section 6, we discuss the implications of our results for future exoplanet searches around giant stars and exoplanet surveys.

2. Sanders 364 and the Proposed Planet

Sanders 364, hereafter S364, is an evolved K giant star, 18 times bigger than the Sun in radius but only 1.35 times more massive. According to color–magnitude and asteroseismic analysis by Stello et al. (2016), S364 is not classified as a red clump star and thus is on the first ascent of the red giant branch. It has not yet passed through the tip of the red giant branch, when the stellar radius would likely have exceeded the size of the orbit for the giant planet reported by B17. They report that the planet has an orbital period of 121 days, and an $m \sin i$ of $1.57 M_{\text{Jup}}$. The stellar parameters of S364 and the orbital parameters of the proposed planet are presented in Table 1.

Table 1
Stellar and Orbital Parameters

Parameter	Value	Units	Source
R.A.	08:49:56.82	hh:mm:ss	(1)
decl.	+11:41:32.99	dd:mm:ss	(1)
Spec. type	K3III	...	(2)
Mass	1.35 ± 0.05	M_{\odot}	(3)
Radius	18.832	R_{\odot}	(1)
T_{eff}	4482 ± 100	K	(4)
$\log g$	2.41 ± 0.1	$\log \text{ cgs}$	(4)
$v \sin i$	4.2 ± 0.5	km s^{-1}	(4)
[m/H]	-0.15 ± 0.08	dex	(4)
P	120.951 ± 0.453	days	(2)
T	2456231.22 ± 4.26	BJD	(2)
e	0.35 ± 0.10	...	(2)
ω	4.444 ± 0.278	rad	(2)
K	56.94 ± 4.26	m s^{-1}	(2)
$m \sin i$	1.57 ± 0.11	M_{Jup}	(2)

Notes. Top: stellar parameters of S364. Bottom: orbital parameters of S364b from B17. P : period; T : time of periastron passage; e : eccentricity; ω : argument of periastron; K : semiamplitude of the RV curve; $m \sin i$: minimum mass.

References: (1) TESS Input Catalog V8.0 (Stassun et al. 2019). (2) B17. (3) Pietrinfermi et al. 2004. (4) SPC fit on TRES spectra (Buchhave et al. 2012, 2014).

3. Observations

3.1. TRES Spectroscopy

We observed S364 with the Tillinghast Reflector Echelle Spectrograph (TRES; Fűrész 2008) 407 times between UT 2011 February 22 and 2022 May 16. TRES is a fiber-fed instrument mounted on the 1.5 m Tillinghast Reflector at the Fred Lawrence Whipple Observatory on Mount Hopkins, Arizona. The first two observations were taken as part of a long-running survey for binaries in M67, and the remaining 405 spectra were acquired with denser sampling starting in 2016, with the goal of better characterizing the planetary system orbiting S364. Typical exposure times were 10–15 minutes, yielding signal-to-noise ratios (S/N) most often between 40 and 80 per resolution element. We obtained Thorium–Argon emission-line spectra before and after the science exposures for wavelength calibration. We optimally extracted the spectra and derived RVs according to the procedures outlined in Buchhave et al. (2010), with the exception that we use the high S/N median observed spectrum as the template for cross correlation, and we account for drifts in the instrument zero-point through nightly monitoring of RV standard stars. As documented in Appendix A, the run-to-run corrections to the velocity zero-point should be good to better than 5 m s^{-1} . The mean internal error of our derived velocities is 15 m s^{-1} . These velocities are reported in Table B1 and plotted in Figure 1. The TRES spectra were also used to derive stellar parameters using the Stellar Parameter Classification tool (SPC; Buchhave et al. 2012). In short, SPC cross correlates an observed spectrum against a grid of synthetic spectra based on Kurucz atmospheric models (Kurucz 1992) to derive effective temperature, surface gravity, metallicity, and rotational velocity. However, we note that the $v \sin i$ value has not been corrected for the contribution by macroturbulence to the line broadening. We report the average stellar parameters in Table 1 from the most recent 52 observations taken in 2022.

3.2. Historical Observations

S364 was observed by the Palomar 200 inch telescope, the Fred Lawrence Whipple Observatory (FLWO) 60 inch Digital Speedometer, the Multi-Mirror Telescope (MMT) Digital Speedometer, and the Oak Ridge Digital Speedometer between 1972 and 1998. From Figure 2, it is clear that S364 has a long history of observation, though the recent TRES observations are of much higher fidelity than the historical observations. The errors of the historical data far exceed the total range of the TRES data, so the historical data unfortunately add very little to the information content of the TRES data. We confirmed this by repeating the analysis in Section 4 on the combined historical and TRES data sets, and there were no statistically significant differences in our results, regardless of the historical data’s exclusion. Thus, we elected to not include the historical data in the final analysis presented in this paper.

Brucalassi et al. (2017) collected observations of S364 from four instruments: HARPS, SOPHIE, HET, and CORALIE. The absolute corrected RVs are plotted with the TRES RVs in Figure 3. Please see Brucalassi et al. (2017) for further details on their RV data.

4. The Search for B17’s Planet

4.1. Lomb–Scargle Periodogram

In this section, we present our search for the 121 days signal detected by B17, utilizing Lomb–Scargle periodograms to identify periodic signals and determine their significance. Figure 4(a) displays the Lomb–Scargle periodogram of S364 over a broad range of frequencies, and Figure 4(b) highlights several notable peaks at low frequencies. The highest peak occurs at a frequency of about 0.00189 day^{-1} , or a period of about 530 days. We also found a smaller peak at a period of 120.7 ± 2.5 days, which is consistent with the 121 days orbital period reported by B17, but at a lower power than the five stronger peaks found at longer periods in our TRES data.

We carried out the same analysis on the published RVs from B17. The resulting Lomb–Scargle periodogram for B17’s data is superimposed onto the periodogram based on our TRES data in Figure 5. The unit of power (y-axis) for the two periodograms are scaled such that the power corresponding to a 0.1% false alarm probability, calculated according to the stationary bootstrap model (discussed in Section 4.2), is the same for both periodograms. Because this is a rough approximation, compare the height of the peaks in the TRES and B17 curves with caution; Figure 5 mainly highlights the differences in the overall shapes of the two periodograms rather than the absolute difference in power between the two periodograms.

While the 121 days peak is nearly the highest peak in the B17 periodogram, the power of the 121 days peak is significantly lower than the power of longer period peaks in the TRES periodogram. One possible explanation is that B17 may not have had a sufficient number and/or density of observations to fully resolve the longer period peaks that are significant in our analysis. The differences between the periodograms at long periods are likely driven by the two different observing cadences, but they may also be influenced by stellar variability at the epochs of observation of each data set.

4.2. False Alarm Probabilities

We calculate the false alarm probability (FAP), or the probability that a signal is a false positive, to determine if the

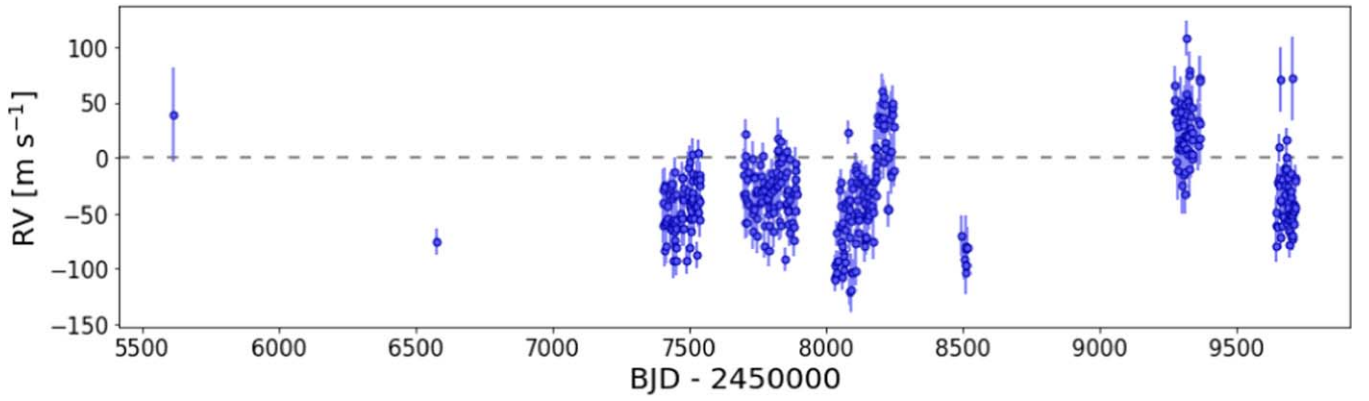


Figure 1. Relative radial velocities for S364 from TRES. In total, we collected 407 RVs over 11 yr, though most of the observations were collected in the latter 6 yr.

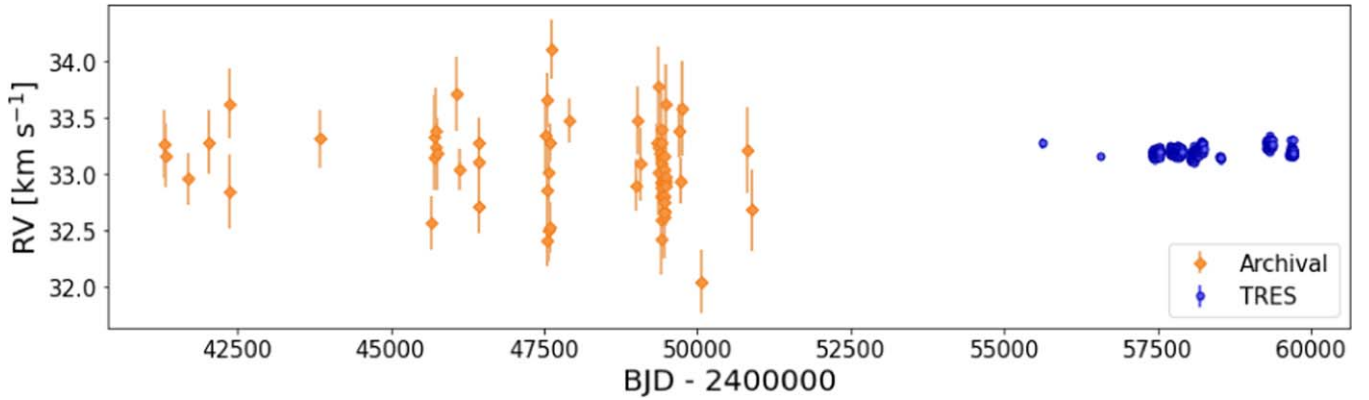


Figure 2. Absolute corrected radial velocities for S364 from historical data and TRES. The error ranges of the historical data far exceed the total range of the TRES data, so we did not include the historical data in the final analysis.

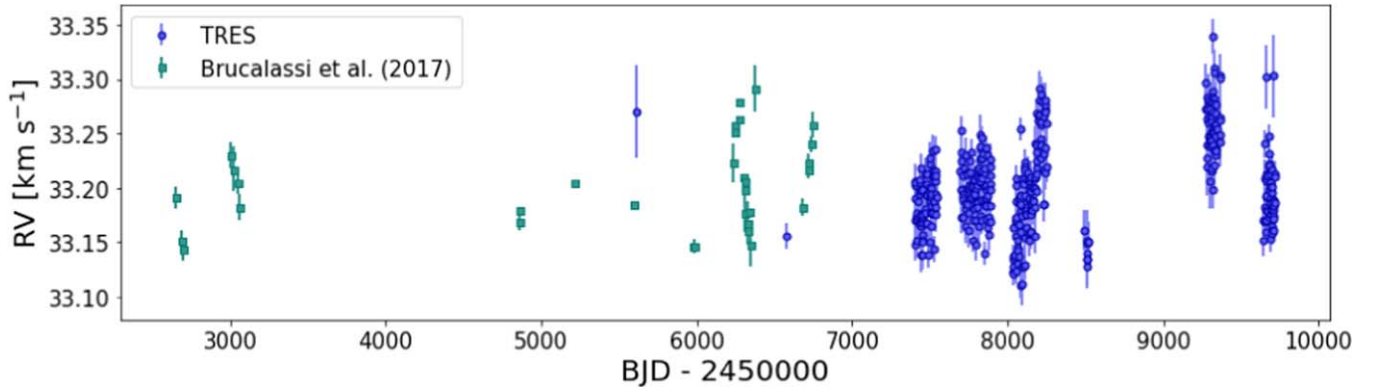
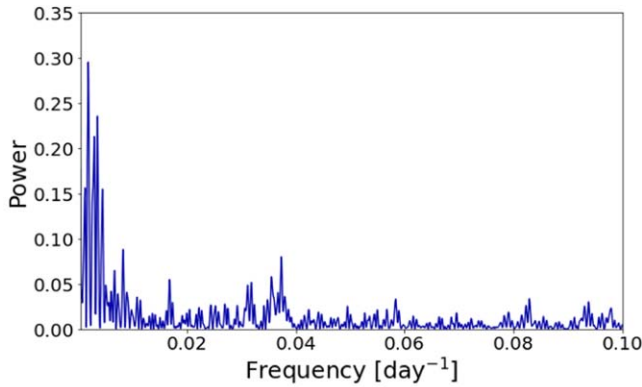


Figure 3. Absolute corrected radial velocities for S364 from B17 and TRES. Both RV data sets span a little over 11 yr, though the TRES data set is more densely sampled, with 407 observations compared to B17’s 32 observations.

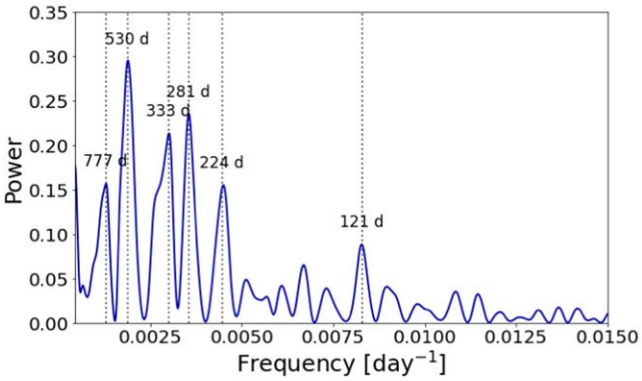
121 days signal discovered in Section 4.1 is statistically significant. We use two variations of the computational bootstrap method: the first is the bootstrap method, and the second is the stationary bootstrap method. The bootstrap method randomly scrambles the order of the RVs, calculates a Lomb–Scargle periodogram from the new mock data set, records the power of the highest peak, and repeats this process to form an array of maximum powers. Then, the cutoffs for a FAP of 5%, 1%, and 0.1% can be calculated by finding the 95th, 99th, and 99.9th percentile powers in that array, respectively. However, the bootstrap FAP calculation is only valid in the presence of uncorrelated noise. Evolved stars are theorized to

have correlated patterns in radial velocity that are not tied to planetary companions, which are speculated to arise from surface features or nonradial pulsations (Hatzes & Cochran 1998; Döllinger & Hartmann 2021). These correlated patterns are considered “red noise,” since they arise from physical phenomena (unlike white noise) but are not related to the potential planetary signal we are trying to observe.

To correct for the influences of “red noise,” we use the stationary bootstrap method from Politis & Romano (1994). The stationary bootstrap uses the same approach as the classical bootstrap method but instead of randomizing the order of the RVs



(a)



(b)

Figure 4. Lomb–Scargle periodograms run on the TRES RVs. There is a peak at a period of about 121 days, within the error range of the period reported by B17. However, there are also five longer period peaks that are more significant than the 121 days peak. (a) Frequency ranges from 0.00043 (corresponding to a period of the length of time we observed S364 regularly) to 0.1. (b) Closer look at longer period peaks; highest peaks are labeled. Frequency ranges from 0.00043 to 0.015.

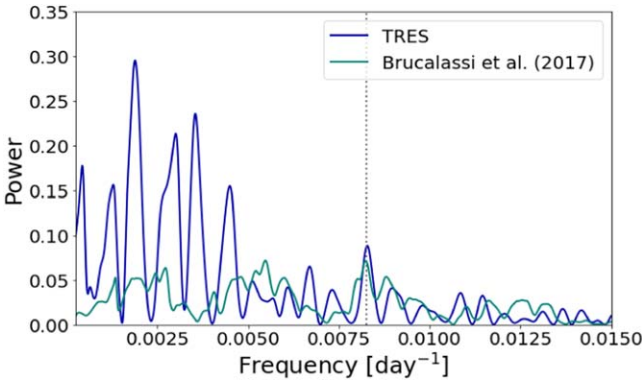
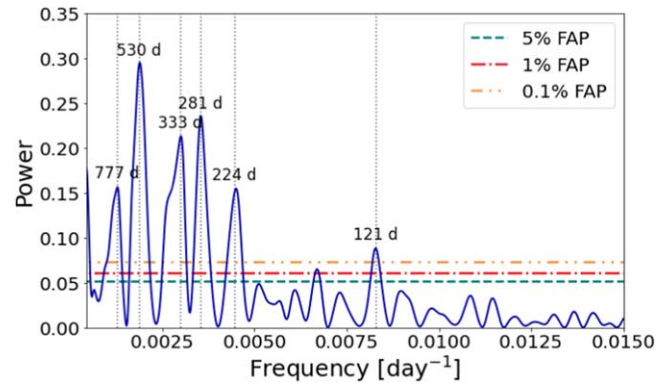
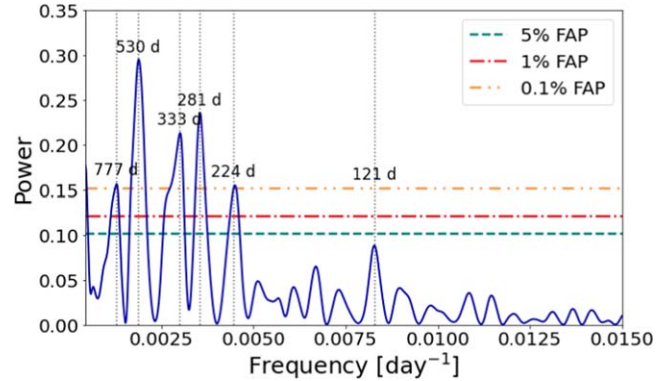


Figure 5. Lomb–Scargle periodogram calculated with the RVs from B17 superimposed on the periodogram calculated with the RVs from TRES, with a dotted vertical line at B17’s reported period of 120.951 days. While the 121 days peak is one of the most significant peaks in the B17 periodogram, it is relatively less significant in the TRES periodogram. Relative power scaled approximately to the 0.1% FAP calculated with the stationary bootstrap method.

individually, the ordered RVs are initially organized into bins of differing lengths, and then the order of the bins is scrambled. The length of each bin is determined by a manually defined initial value p and follows a geometric distribution. By scrambling RVs binned



(a) Bootstrap method.



(b) Stationary bootstrap method.

Figure 6. Figure 4(b) with the addition of dashed horizontal lines corresponding to FAPs of 5%, 1%, and 0.1%. The dotted vertical lines highlight the long-period peaks identified in Section 4.1. Using the bootstrap method, the 121 days peak passes the 0.1% FAP level, while using the more robust stationary bootstrap method, the 121 days peak does not even pass the 5% FAP level.

over different timescales, we can account for the presence of correlated noise at different periods in our FAP calculations. A limitation of the stationary bootstrap method is that the probability of sampling smaller or larger bins requires a manually defined initial value p (Politis & Romano 1994). A lower p corresponds to a higher probability of sampling longer bins, and vice versa. In this analysis, our chosen value of p was 0.1, favoring longer bins since our periodogram (Figure 4(b)) revealed apparent long timescale periodicities.

Figure 6(a) displays a plot of the original Lomb–Scargle periodogram with horizontal lines at FAPs of 5%, 1%, and 0.1% calculated with the bootstrap method, while Figure 6(b) displays a plot with horizontal lines at FAPs of 5%, 1%, and 0.1% calculated with the stationary bootstrap method. The periods that correspond to the peaks with a bootstrap FAP of 0.1% or lower are listed in Table 2. The peaks that also pass the 0.1% stationary bootstrap FAP level are starred. The only peak that passes the bootstrap 0.1% FAP level but does not pass the stationary bootstrap 0.1% FAP level is the 121 days peak. In Figure 6(a), the peak at 121 days has a FAP just under 0.1%, while in Figure 6(b), that same peak has a FAP much greater than 5%. In other words, using the bootstrap method, the 121 days peak appears to be significant, while using the stationary bootstrap method, it does not. Thus, it appears that when accounting for correlated noise, the 121 days peak is not significant. The longer period peaks that pass the 0.1% FAP level will be discussed further in Section 5.

Table 2
Significant Long-period Peaks

Period (day)	Frequency (1/day)	Error (1/day)	Power
120.7	0.00829	0.000344	0.088
223.5*	0.00447	0.000409	0.154
280.9*	0.00356	0.000337	0.235
333.2*	0.00300	0.000324	0.213
530.4*	0.00189	0.000412	0.293
777.3*	0.00129	0.000346	0.156

Note. Long-period peaks from the TRES Lomb–Scargle Periodogram that have a higher power than the 121 days peak. Starred periods correspond to peaks that pass the 0.1% stationary bootstrap FAP level. Errors are calculated using the FWHM of the periodogram peak.

4.3. Signal Power Analysis

If an RV signal arises from orbital motion, we expect the signal to monotonically increase in significance as more observations are included in the analysis, while a quasiperiodic RV signal would exhibit fluctuations in significance. One way to test this is a stacked Lomb–Scargle periodogram, as proposed by Mortier & Collier Cameron (2017). We start by calculating a Lomb–Scargle periodogram on the first 200 observations collected by TRES. Then, we calculate another periodogram after a subsequent observation is added, and we repeat until all the observations are included. Figure 7 plots the stacked periodogram, with the number of observations, starting at 200 and ending at 407 (the total number of observations), on the y -axis against the frequency on the x -axis. The power is color coded: darker red indicates higher power, and lighter red or white indicates lower power. The 121 days peak appears to grow in strength up to about 350 observations, but then the growth wavers and even decreases slightly with additional observations, unlike what we would expect from a signal of orbital motion.

However, it can be difficult to decipher slight changes in color intensity in the stacked Lomb–Scargle periodogram, so another way to see this phenomenon is by plotting the evolution of the power of a specific peak as observations are added. This method of analysis was first employed by Hatzes (2013) to refute the planet GL 581g. Our analysis is also inspired by Reichert et al. (2019), particularly by Figure 5 where the signal power evolution is plotted in chronological order and reverse chronological order. Since the peaks have some width, we calculate the periodogram for a small range of frequencies around 0.00829 (corresponding to a period of 121 days) based on the error range (listed in Table 2). The power plotted is the maximum power within this range. Data points are added in increments of 10 and in chronological (top) and reverse chronological order (bottom). For comparison, we apply this analysis to a simulated RV data set with an injected 121 days planet based on B17’s reported orbital parameters, with the average instrumental errors for TRES assigned to each RV data point. In the top panel of Figure 8, the power of the 121 days peak in the simulated data set increases with the number of observations, while the power of the 121 days peak has a slightly downward trend between $N=200$ and $N=250$, slightly increases between $N=250$ and $N=350$, then trends flat or slightly downward for the last ~ 50 observations added. In the bottom panel of Figure 8, the power of the 121 days peak in the simulated data set similarly increases with the number of observations, while the power of the real 121 days signal shows

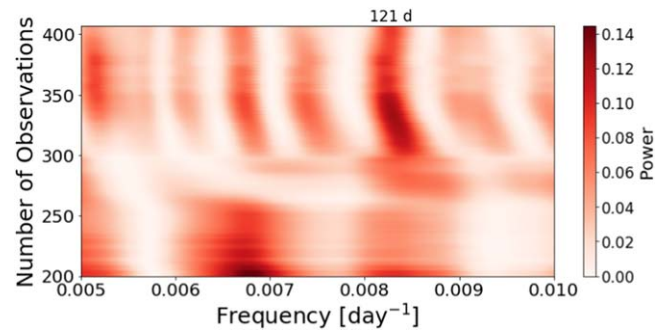


Figure 7. Stacked Lomb–Scargle periodogram. The color bar on the right denotes the relationship between color intensity and power. The 121 days signal does not exhibit a monotonic growth in power that would be characteristic of orbital motion.

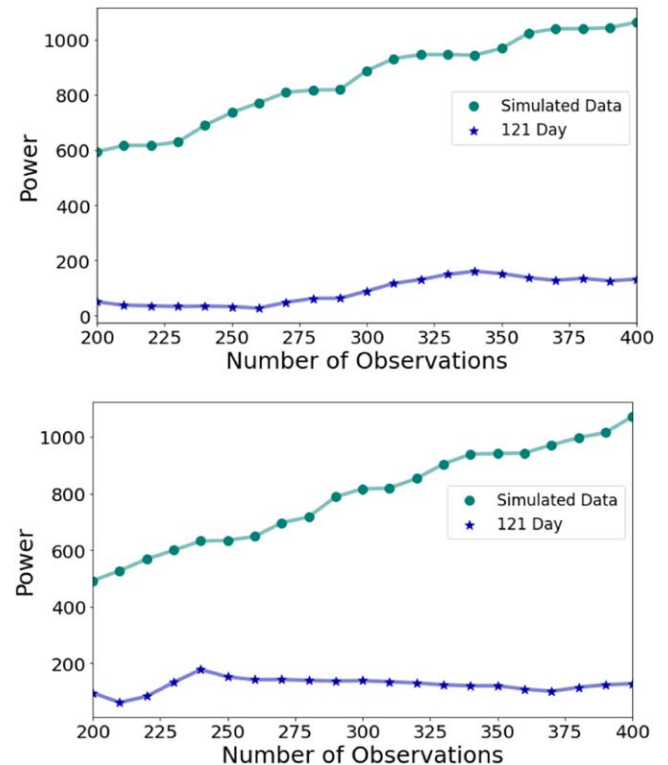


Figure 8. Evolution of Lomb–Scargle periodogram power as a function of the number of observations for the 121 days signal. For comparison, the same is plotted for simulated data using B17’s orbital parameters. Top: data points are added in increments of 10 and in chronological order. Bottom: data points are added in increments of 10 and in reverse chronological order. While the power of the simulated peak grows with more observations, the power of the real 121 days signal does not show a consistent growth in power.

significant dips and an overall decrease in power as observations are added, indicating that the 121 days signal decreases in power when adding older data. Thus, we again conclude that the signal does not appear to exhibit characteristics of orbital motion, though we cannot fully rule out the existence of the 121 days planet based on signal power analysis alone.

4.4. Orbital Model

In addition to the periodogram analysis, we compare the phase-folded TRES RVs to the orbit predicted by B17 in Figure 9. We model the orbit of B17’s proposed planet by predicting the stellar RVs based on the published orbital parameters using the RV fitting

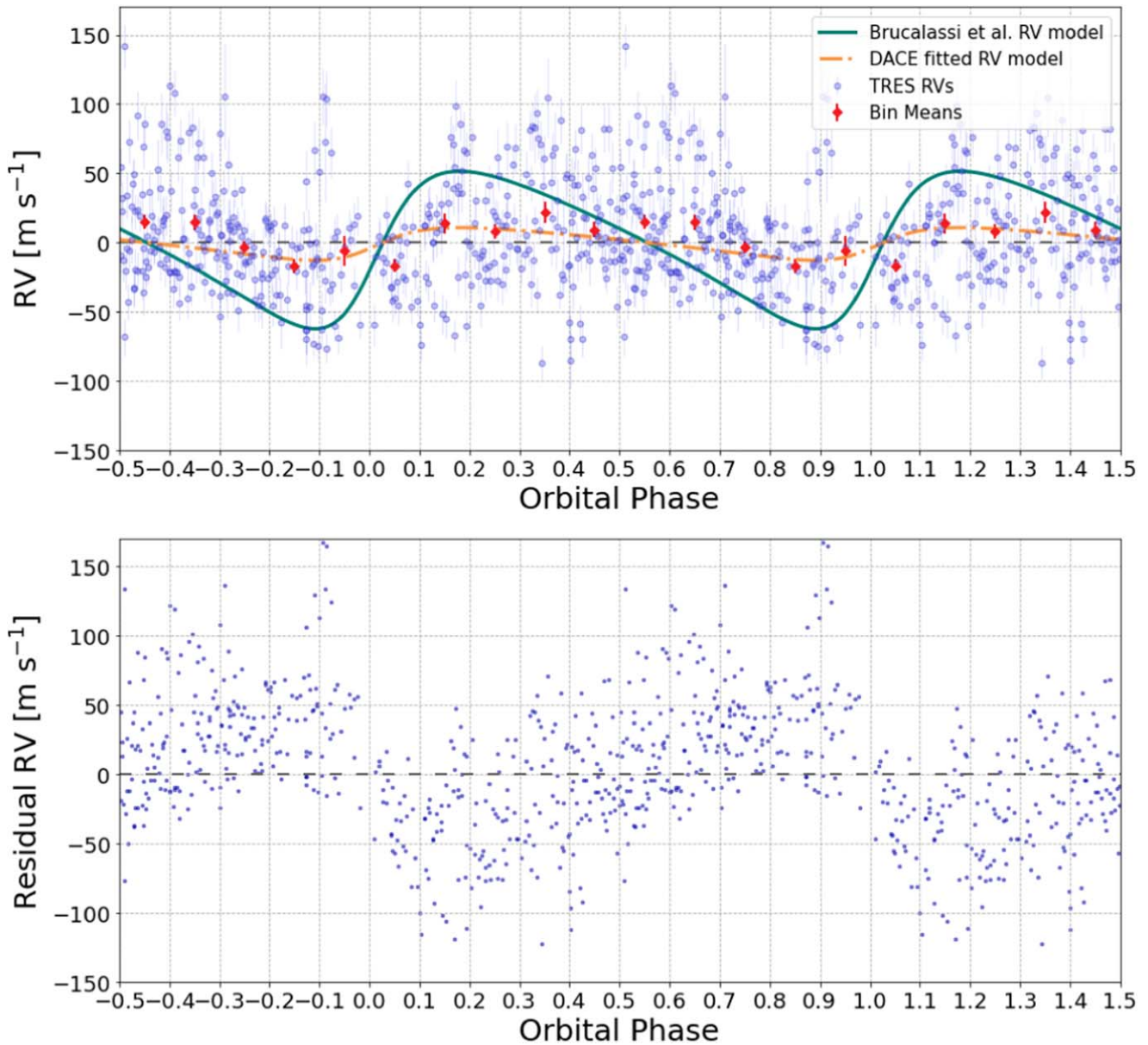


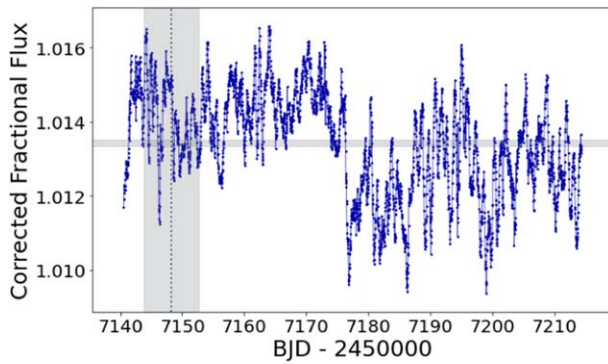
Figure 9. Phase-folded TRES data overlaid over the predicted relative RV curve based on B17’s 121 days planet parameters after fitting for the gamma velocity (top) and the associated residuals of the TRES RVs and B17’s predicted RV curve (bottom). The orange dashed–dotted curve is an RV curve fitted to TRES data with the semiamplitude as a free parameter using DACE. The TRES RVs and binned means do not fit well to B17’s predicted RV curve, and the DACE-fitted curve has a significantly lower amplitude. Thus, our observations and analysis do not support B17’s planet discovery.

toolkit Radvel (Fulton et al. 2018). We plot the predicted RV curve over two orbital periods, corresponding to an orbital phase from -0.5 to 1.5 , in teal. We phase fold the TRES data according to B17’s proposed ephemeris and plot it over the predicted RV curve, represented by the smaller, blue points. The larger, red points are the mean velocities for each RV bin, with 20 bins evenly spaced in phase space. We also plot the residuals for the TRES data from the predicted curve in the bottom plot. Using the RV module from the Data & Analysis Center for Exoplanets (DACE), we fit a 121 days orbital solution to the TRES data with the time of periastron, argument of periastron, and eccentricity set to the values reported in B17, and the semiamplitude and gamma velocity set as free parameters. We plot the DACE-fitted curve for comparison in Figure 9, represented by the orange dashed–dotted curve. Our best-fit semiamplitude was 11.79 m s^{-1} , compared to B17’s semiamplitude of 56.94 m s^{-1} .

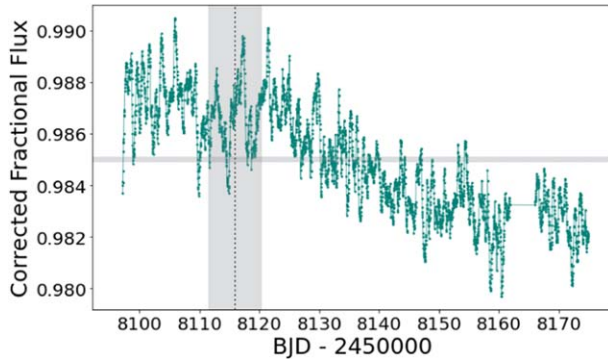
Our data do not fit well with the predicted RV curve, as evidenced by the strong pattern of residuals. However, there does appear to be some weak modulation in the TRES data that matches the B17 ephemeris: the bin means between the phases of 0.6 and 1.0 seem to dip in parallel with the predicted RV curve. This may partially explain the 121 days peak we observe in our periodogram. However, the combined results of our analysis—the presence of stronger peaks at longer periods, the overall deviation of the TRES RVs from the predicted RV curve, and the low amplitude of the DACE orbital fit—strongly suggest that the proposed planet model cannot fully explain what we observe in the RVs.

4.5. Photometric Data from K2

We were also able to obtain light curves of S364 from the several campaigns of the K2 mission (Howell et al. 2014;



(a) Campaign 5



(b) Campaign 16

Figure 10. K2 light curve plots, with a dotted vertical line at the predicted transit time based on B17’s orbital parameters and a vertical shaded window of 8.86 days centered on the transit times, representing the transit duration. The narrow horizontal shaded window is a reference for the expected transit depth for a Jupiter-sized planet centered on the average flux in the window.

Vanderburg & Johnson 2014; Vanderburg et al. 2016). To search these light curves for signals of B17’s proposed planet, we first needed to calculate the predicted depth and length of transit, the times of transit, and the uncertainty in the predicted times of transit based on the proposed orbital parameters given in Table 1.

To calculate an approximate transit duration, we found the radius of S364 in the TESS Input Catalog, which was about 18.8 solar radii. Using the stellar parameters for S364 and assuming a circular orbit, the maximum transit duration we calculated was approximately 6.27 days, assuming that the planet transits the entire diameter of the star from our point of view. To account for the significant eccentricity of the proposed orbit, we multiplied the previous transit duration by an “eccentricity” factor derived in Burke (2008), and we found a maximum duration of 8.86 days.

We used NASA’s Transit and Ephemeris Service (Akeson et al. 2013) to calculate the predicted times of transit. Two of those times were within the time frames in which we had K2 data. However, the uncertainties for those transit times were on the scale of several days, so it was challenging to differentiate a dip of planetary origin from noise in the light curve.

To estimate transit depth, we calculate the ratio between the cross-sectional area of the planet and that of the star. If we assume that the proposed planet had a radius similar to Jupiter, we would only expect to see a 0.003% change in brightness, since the radius of the star far exceeds the radius of the planet. Even if the planet had a radius twice that of Jupiter, we would only expect to observe a 0.013% change in brightness. Unfortunately, the noise of the K2 flux curves, very likely

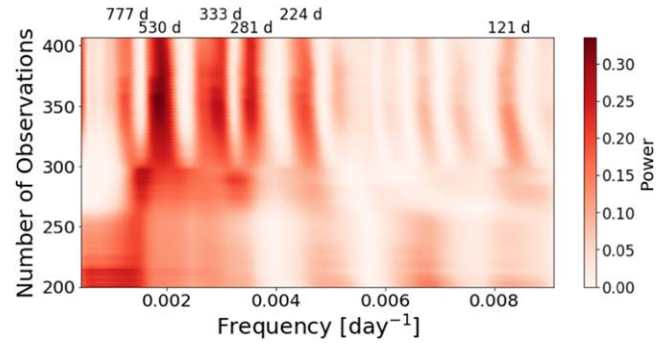


Figure 11. Stacked Lomb–Scargle periodogram. The color bar on the right denotes the relationship between color intensity and power. The periods of the most significant peaks are labeled. None of the signals appear to exhibit monotonic growth in power that would be characteristic of orbital motion.

caused by pulsations and granulations on the star, would easily obscure this small change in brightness.

Figure 10 displays the plots of the K2 Campaign 5 and Campaign 16 light curves, with a gray dotted line at the predicted midtransit times. The vertical shaded window is a reference for the transit duration of 8.86 days centered on the predicted midtransit times. The narrow horizontal shaded window is a reference for the expected transit depth for a Jupiter-sized planet, centered on the average flux in the window. From the plot, we can see that it would be nearly impossible to detect a transit of B17’s proposed planet from the K2 data.

5. Potential Long-period Planets

As we can see from the Lomb–Scargle periodogram (Figure 4) and FAP levels (Figure 6), there are five long-period signals that are more significant than the 121 days signal. In this section, we will analyze whether these signals are potential planet candidates following the line of analysis used for testing the 121 days signal, as well as additional analysis of the window function and aliasing.

5.1. Signal Power Analysis

Briefly, from Section 4.2, we find five long-period signals that have a FAP under 0.1%, at periods of 224, 281, 333, 530, and 777 days (Table 2). Again, if an RV signal arises from orbital motion, we expect the signal to monotonically increase in significance as we add more observations to the analysis. To test this for the long-period signals, we plot a stacked Lomb–Scargle periodogram for a wider range of frequencies in Figure 11.

The growth in power of the 224, 333, 530, and 777 days peaks stagnate and ebb after around 350–375 observations, similar to the 121 days peak in our earlier analysis. Thus, according to this metric, none of the significant long-period signals, as determined by our FAP calculations, exhibit a monotonic growth in power that is characteristic of orbital motion. Interestingly, it appears that a minimum observation baseline of about 300 observations, which corresponds to a time baseline of about 10 yr for our data set, is required for the longer period peaks to be resolved. We speculate that although B17 may have had a long enough time baseline, they may not have had dense enough data to fully resolve these longer period peaks.

Using the same procedure as described in Section 4.3, we plot the evolution of the power of each peak. Figure 12 displays the power versus number of observations plots for the six significant peaks identified in Table 2, as well as for the

Table 3
Orbital Parameters for the Best-fit Solutions from DACE

P_f (d)	P_p (d)	T (BJD)	e	ω (rad)	K (m s $^{-1}$)	γ (m s $^{-1}$)	$M \sin i$ (M_{Jup})
119.270	120.664	2455409.568	0.720	2.759	25.311	-34.08	0.520
220.967	223.519	2455350.540	0.465	0.555	28.499	-33.92	0.917
279.451	280.893	2455410.041	0.571	0.094	44.508	-28.39	1.435
332.107	333.233	2455323.460	0.343	0.753	39.937	-22.35	1.561
552.250	530.401	2455432.877	0.641	5.773	40.753	-32.23	1.541

Note. Each solution is at or near the periods listed in Table 1. The 777 days period is excluded because DACE’s Keplerian fit did not converge for this period. P_f : best-fit period found by DACE near the peak in the periodogram, P_p : period at which the periodogram has a peak (listed in Table 1), T : time of periastron passage, e : eccentricity, ω : argument of periastron, K : semi-amplitude of the RV curve, γ : gamma velocity.

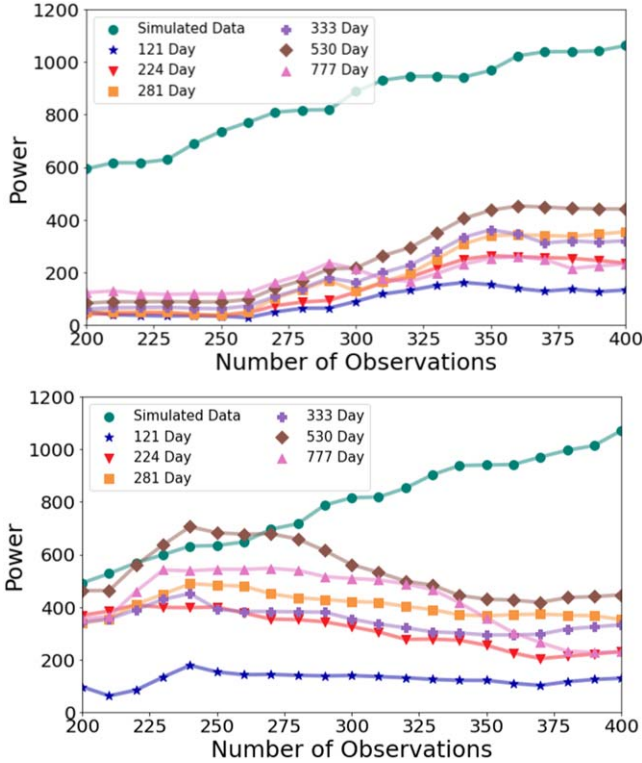


Figure 12. Evolution of Lomb–Scargle periodogram power as a function of the number of observations for the long-period signals. Simulated data is again using B17’s orbital parameters, with the average instrumental errors for TRES added. Top: data points are added in increments of 10 and in chronological order. Bottom: data points are added in increments of 10 and in reverse chronological order. The power of the long-period peaks alternate in relative significance and show significant dips in both plots, suggesting that these signals are unlikely to be evidence of orbital motion.

injected planet. None of the curves in Figure 12 exhibit the steadily increasing power that would be expected from orbital motion, though we cannot fully rule out the existence of (a) planetary companion(s) based on signal power analysis alone.

5.2. Orbital Models

We use DACE to fit Keplerian orbits to the periods listed in Table 2 to determine if orbital solutions could explain these periodic signals. The predicted RV curves and phase-folded TRES RVs based on the respective ephemerides are plotted in Figure 14. The best-fit orbital parameters are listed in Table 3.

The 777 days period is excluded because DACE’s Keplerian fit did not converge for this period. Our orbital fits are unlikely to be evidence of real planets since many of the orbital fits have

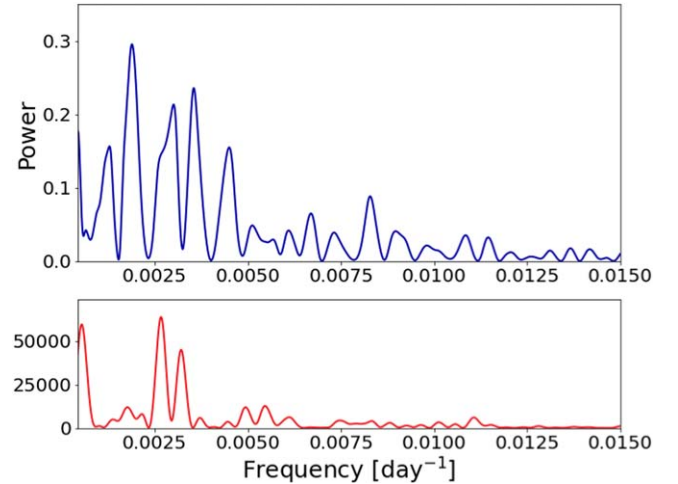


Figure 13. TRES Lomb–Scargle periodogram (top) and corresponding window function calculated from the TRES times of observations (bottom).

high eccentricities and similar semi-amplitudes. These characteristics are often found in orbital fits to correlated patterns of RV variation that are quasiperiodic and not planetary in origin.

We also investigated the possibility of a multiplanet fit using DACE. First, we fitted a Keplerian orbit to one of the significant peaks listed in Table 2. Then, we fitted a second Keplerian orbit to one of the significant peaks in the residual periodogram. Occasionally, a third fit was needed to remove all significant peaks from the residual periodogram. We repeated this procedure for every period in Table 2. DACE also calculates the Bayesian Information Criterion (BIC) for each orbit. For the multiplanet fits with the lowest BICs and most convincing fits (i.e., eccentricity was not close to 1), we use REBOUND, an N -body integrator (Wisdom & Holman 1991; Rein & Liu 2012; Rein & Tamayo 2015), to dynamically model the system. All of the two- or three-planet systems suffered from long-term instability, and many systems suffered from a planet ejection within a few hundred or even tens of orbits. This was unsurprising because many of the orbits fitted in this manner had high eccentricities.

5.3. Window Function

We investigated whether any of the signals in the periodogram could be linked to aliasing with the window function. The window function is related to the uneven time spacing of the observations. According to Dawson & Fabrycky (2010), “an alias is a convolution in frequency space of a physical frequency with the window function.” In frequency space,

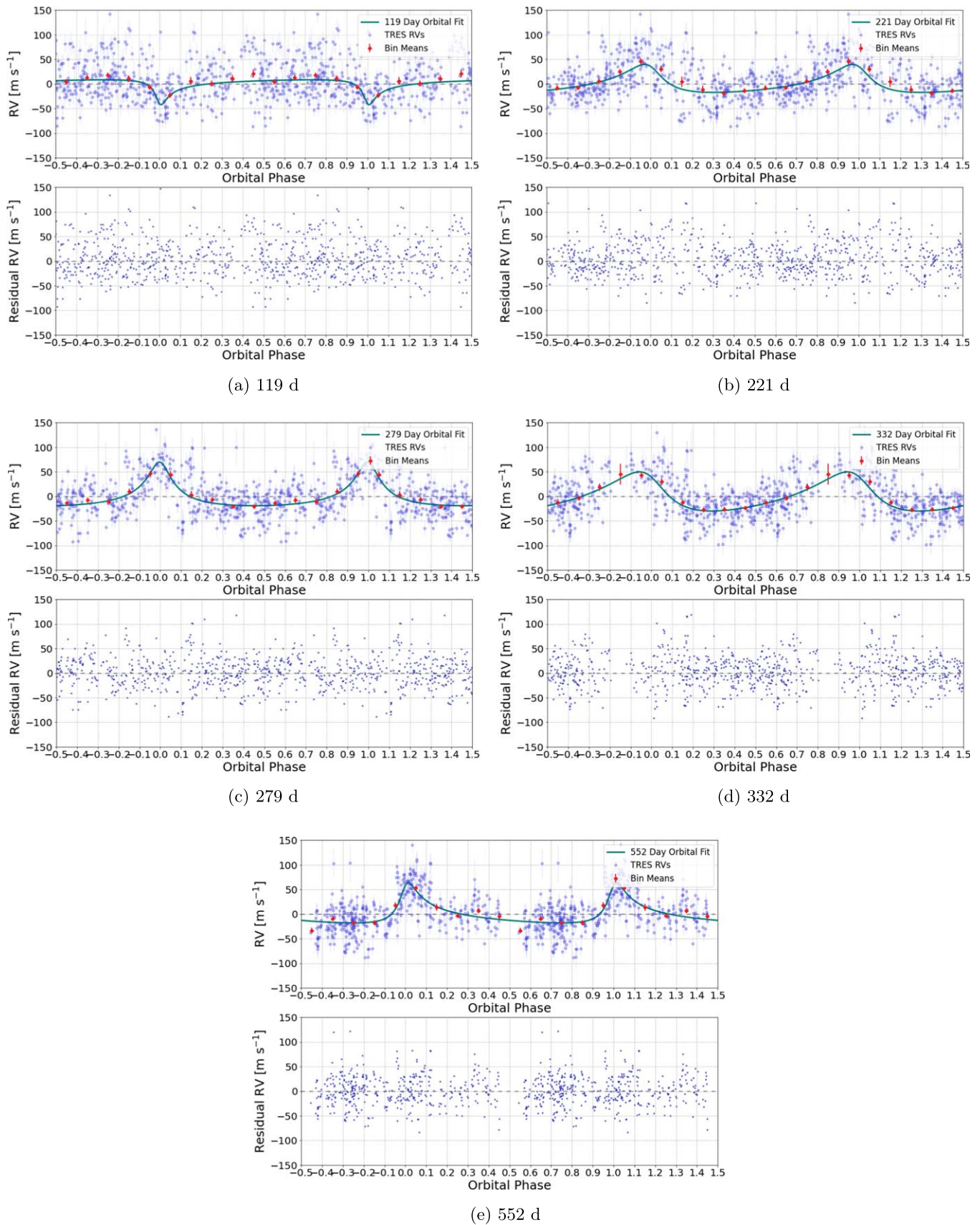


Figure 14. Phase-folded TRES data overlaid over the predicted relative RV curves from DACE for the longer period peaks in Table 2 (top) and the associated residuals of the TRES RVs and DACE’s predicted RV curves (bottom). The orbital fits seem unconvincing due to the high eccentricities and similar semiamplitudes across all of the fitted periods.

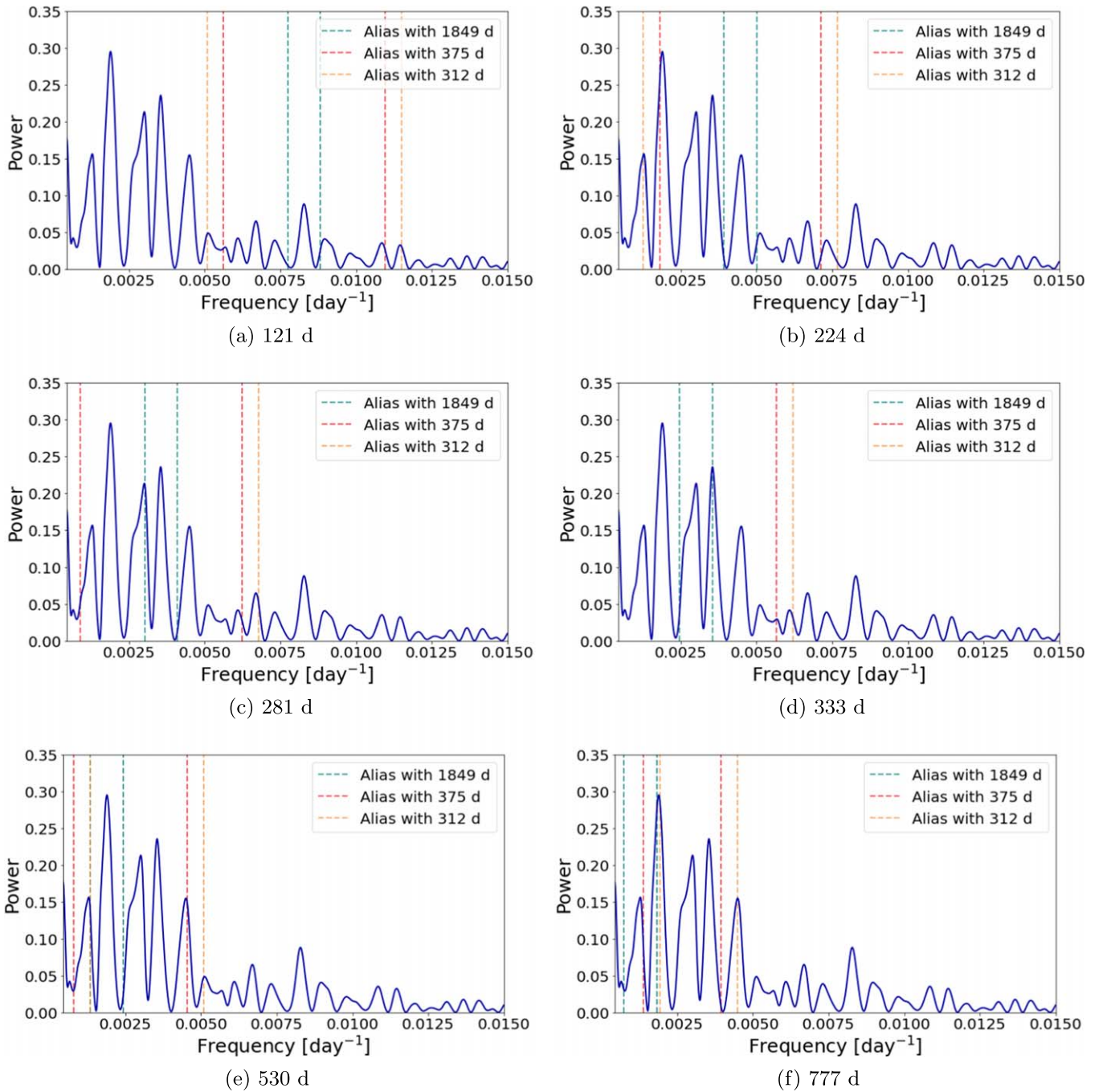


Figure 15. Aliasing of the window function and the periodogram signals. The Lomb–Scargle periodogram from the TRES data is plotted in solid blue. The dashed vertical lines indicate where we would expect a spurious peak to occur in the periodogram from a convolution of a peak in the periodogram (period labeled underneath the figure) and one of the three strongest peaks in the window function (labeled by color).

spurious signals can occur at $f = |f_p \pm f_w|$, where f is the frequency of the spurious signal, f_p is the frequency of the physical signal, and f_w is the frequency of the window function peak. Figure 13 plots the TRES periodogram and the window function. The top three peaks in the window function occur at 1849 days ($0.000541 \text{ day}^{-1}$), 375 days ($0.002667 \text{ day}^{-1}$), and 312 days ($0.003209 \text{ day}^{-1}$).

The difficulty in interpreting the window function and the resulting aliasing is determining which signal(s) is (are) the real, physical signal(s). Dawson & Fabrycky (2010) proposed a method for determining the “real” peak(s), but it involves analyzing the phases of the signals, which does not work well

for quasiperiodic data since the phases are not well defined. It is quite likely that one or two of the significant peaks in the TRES periodogram arise from real quasiperiodic variations in the RVs, but it is much less likely that all of the peaks are physical signals. Determining a real signal is even more difficult when looking for long-period signals, since observations necessarily must span multiple seasons to confirm such a signal. When observations span multiple seasons, seasonal window functions will inevitably manifest. We can see this in our window function—two of the highest peaks occur at periods of 315 days and 375 days, which are both close to one year. Even worse, the aliases with seasonal window functions often

appear in the same period range as the periodic signals we are looking for. In other words, when long-period signals interact with the seasonal window function, they tend to produce long-period aliases as well. Thus, we are not able to confidently determine which of the periodic signals discovered in the TRES periodogram is the “real” signal, but Figure 15 and Table 4 shows some of the possible relationships between the window function and the real data.

6. Discussion

6.1. Exoplanet Occurrence Rates

The significance of B17’s reported discovery of a planet orbiting S364 is rooted in their subsequent calculation of exoplanet occurrence rates. B17 reports that the occurrence rate of giant planets with a period between 1 and 1000 days and mass between 0.2 and 10 Jupiter masses orbiting evolved stars is $23.0\%_{-15.0}^{+29.9}$. This occurrence rate is based on Brucalassi et al.’s (2017) discovery of two giant planets in M67: one of which is discussed here (Sanders 364) and the other is around a similar K4III star in M67, Sanders 978 (Brucalassi et al. 2017). The reported giant planet orbiting Sander 978 has a long period of 511 days and a semi-amplitude of 45 m s^{-1} . One has to wonder if the planet around Sanders 978 is also vulnerable to a fate similar to our results for Sanders 364. Unfortunately, it appears that our results suggest that the occurrence rate for giant planets orbiting K giants in M67 is not well constrained.

Grunblatt et al. (2019) establish that the occurrence rate of close-in giant planets with a period between 3.5 and 10 days and a radius between 1 and 2 Jupiter radii around evolved stars is $0.49\% \pm 0.29\%$ using RV and transit observations. Grunblatt et al. (2019) identify that this rate is within the error range of the rate expected for planets in that parameter space around main-sequence stars, which is $0.15\% \pm 0.06\%$ (Howard et al. 2012). It is important to note that Grunblatt et al.’s (2019) sample of evolved stars has similar masses and metallicities to the sample of main-sequence stars used to derive the occurrence rate in Howard et al. (2012). Thus, the Howard et al. (2012) sample of main-sequence stars can reasonably represent a population of progenitors to the evolved population in Grunblatt et al. (2019). Since the occurrence rates for these two samples are similar, the Grunblatt et al. (2019) results suggest that the occurrence rate for short-period planets does not change as populations of stars evolve off of the main sequence and up the giant branch.

However, Döllinger et al. (2009) find that long-period giant planets are more common around giant stars ($\sim 10\%$ occurrence rate, even up to $\sim 15\%$) compared to main-sequence (MS) stars ($\sim 5\%$ occurrence rate, Cumming et al. 2008). All of the planet discoveries reported by Döllinger et al. (2009) have periods greater than 150 days, so it appears that Döllinger et al.’s (2009) survey focuses on a different parameter space than Grunblatt et al. (2019). It is unclear whether the main-sequence occurrence rate from Cumming et al. (2008) is derived from a population that could reasonably represent a population of progenitors, so we may not be able to view these occurrence rates from an evolutionary point of view as we did with Grunblatt et al.’s (2019) results. It is also possible that the differences in the masses, metallicities, etc., of the stars surveyed create a discrepancy between the two occurrence rates.

However, assuming that the planet occurrence rates from Cumming et al. (2008) are derived from corresponding main-sequence “progenitor” stars to the evolved stars in Döllinger et al. (2009), there appears to be a tension between the Döllinger et al. (2009) and Grunblatt et al. (2019) results. Given current planet formation theories, it would not be expected that evolved stars would have more long-period planets than main-sequence stars but the same number of short-period planets. In a more recent paper, Döllinger & Hartmann (2021) describe the apparent intrinsic RV variations present in many evolved K giant stars, and they propose that this discrepancy in the calculated occurrence rates between giant stars and MS stars may be due to false positive detections of long-period planets among the giants. Past false positive planets around evolved stars with long periods cited in Döllinger & Hartmann (2021) include 42 Dra, γ Dra, and Aldebaran, which will be discussed further in Section 6.2. Our work may add another false positive to this list.

6.2. Long-period Variations in Evolved Stars

In our Lomb–Scargle periodogram, we observe high peaks at long periods, on the order of approximately 100 to 800 days. Previous studies on long-period RV variations in giant stars include a series of papers by Artie Hatzes and William Cochran (Hatzes & Cochran 1993, 1996, 1998, 1999; Hatzes et al. 2006). Hatzes & Cochran (1993) present precise RVs of three K giants: Arcturus, Pollux, and Aldebaran, which all have similar spectral types and masses to S364. Their analysis finds RV variations with periods of 233, 558, and 643 days, respectively. Hatzes & Cochran (1993) calculate similar planetary orbital periods and masses for each star. They note that this apparent coincidence may be an indication that these RV variations are inherent to K giants or another characteristic shared by the three stars, rather than evidence of planetary companions. Combining the results of their 1993, 1998, and 1999 papers, Hatzes and Cochran report a total of seven K giants that have periodic RV variations on the order of 200–600 days.

Reichert et al. (2019) refute the 629 days candidate planet reported to orbit Aldebaran, one of the K giants reported in Hatzes & Cochran (1993) and Hatzes et al. (2015). When they combined new data from the Lick Observatory with the data from Hatzes et al. (2015), the proposed orbital solution fit poorly to the data. However, an analysis of the Lick data reveals a peak around 587 days that cannot be fully explained by an orbital solution.

Additionally, Döllinger et al. (2006) report that in a sample of 62 G and K giants, nine stars (15%) exhibit long-period RV variations of uncertain origin. The periods are on the order of hundreds of days.

6.2.1. Active Regions

One proposed idea for a source of the long-period RV signals observed in these studies is active regions on the star (Hatzes & Cochran 1993). Surface features like plages and spots are known to affect spectral line profiles in ways that mimic periodic variations characteristic of planetary companions (Dumusque et al. 2014). The quasiperiodicity of these surface feature signals is tied closely to the rotational period of the star. Evolved giant stars generally have longer rotational periods compared to main-sequence stars due to a few

Table 4
Possible Relationships between TRES Periodogram Signals (s) and the Window Function (w)

Period (d)	Frequency (day ⁻¹)	Potential Aliases
120.7	0.00829	...
223.5	0.00447	530 day (s) & 375 day (w) 777 day (s) & 312 day (w)
280.9	0.00356	333 day (s) & 1849 day (w)
333.2	0.00300	281 day (s) & 1849 day (w)
530.4	0.00189	224 day (s) & 375 day (w) 777 day (s) & 312 day (w)
777.3	0.00129	777 day (s) & 1849 day (w) 224 day (s) & 312 day (w) 530 day (s) & 1849 day (w) 530 day (s) & 312 day (w)

mechanisms that act on them during the star’s evolution over time. For example, stars with masses close to that of the Sun experience braking from stellar magnetic winds as they age along the main sequence (Kawaler 1988; Barnes 2003). In addition, a star’s moment of inertia increases as it turns off of the main-sequence branch and swells in size to become a giant (Ceillier et al. 2017). Furthermore, the size of the surface convection zone grows as the star evolves to cooler temperatures, and convection is thought to play a critical role in the braking mechanism.

From Choi et al.’s (1995) sample of 12 G and K giant stars, the authors find that eight of the stars had rotation periods between 100 and 200 days, so it is plausible that a K giant like S364 could exhibit spectral variations with a periodicity on the order of magnitude of the 121 days signal, though this theory does not help explain the longer period signals.

However, Brucalassi et al. (2014) find that S364 exhibits very low variability ($\sim 2\%$) in $H\alpha$, which suggests that chromospheric activity levels are relatively low. If there are long-lived spots or plages on the surface, we would expect to see higher variability in $H\alpha$. While we cannot eliminate exotic stellar active regions as an explanation for the long-period signals, it is unlikely that stellar active regions tell the full story of S364.

6.2.2. Pulsations and Oscillations

Hatzes & Cochran (1993, 1998, 1999) do not exclude the possibility of planetary companions, but they suggest that oscillations or pulsations are a more likely explanation for the long-period variations in the evolved stars they observed. Radial pulsations are excluded since the expected radial pulsation periods for K giant stars at the fundamental mode and the first two harmonics are under 10 days (Hatzes & Cochran 1993). However, nonradial pulsations may be able to produce RV variations on timescales of hundreds of days.

Reichert et al. (2019) speculate that the long-period RV variations are intrinsic to K giants, possibly arising from oscillations/pulsations or dipole oscillatory convective modes (Saio et al. 2015). The oscillatory convective modes described in Saio et al. (2015) result from oscillations in the outermost layers of the deep convective zone of luminous red giant stars. However, it is unclear whether this phenomenon applies to S364 since its luminosity is slightly less than the minimum luminosity considered in the paper.

7. Conclusion

In summary, this paper is not a criticism of B17’s analysis but rather a cautionary tale about detecting planets around K giants and evolved stars that exhibit intrinsic RV variations. Rich, well-sampled data sets are needed to combat the influence of correlated noise that can mimic planetary signals. Analysis techniques like stacked Lomb–Scargle periodograms and plotting signal power evolution against the number of observations, as well as analysis of aliasing with the window function, can help discern planetary signals from signals of other origins. In the case of Sanders 364, using these methods on a dense RV data set revealed no convincing evidence for the planet reported by B17, though we cannot fully exclude the possibility of one or more planetary companions at another period(s). Even so, we find that planetary and multiplanetary solutions cannot fully explain the RV variations we detect in our data. We theorize that K giants may exhibit inherent quasiperiodic stellar variations that can masquerade as planetary signals. Thus, we suggest that exoplanet detections around K giants be treated with caution. Additional observational follow-up and analytical validation should be used to confirm these detections. Further investigation of K giant stars can better characterize the origins of these long-period RV variations.

Acknowledgments

This publication makes use of The Data & Analysis Center for Exoplanets (DACE), which is a facility based at the University of Geneva (CH) dedicated to extrasolar planets data visualization, exchange, and analysis. DACE is a platform of the Swiss National Centre of Competence in Research (NCCR) PlanetS, federating the Swiss expertise in Exoplanet research. The DACE platform is available at <https://dace.unige.ch>.

Simulations in this paper made use of the REBOUND *N*-body code (Rein & Liu 2012). The simulations were integrated using WHFast, a symplectic Wisdom–Holman integrator (Wisdom & Holman 1991; Rein & Tamayo 2015).

In addition, this research has made use of the NASA Exoplanet Archive, which is operated by the California Institute of Technology, under contract with the National Aeronautics and Space Administration under the Exoplanet Exploration Program (NASA Exoplanet Science Institute 2020).

Furthermore, this paper includes data collected by the Kepler mission and obtained from the MAST data archive at the Space Telescope Science Institute (STScI). Funding for the Kepler mission is provided by the NASA Science Mission Directorate. STScI is operated by the Association of Universities for Research in Astronomy, Inc., under NASA contract NAS 5-26555.

The authors thank the Harvard College Research Program, the Office of Undergraduate Research and Fellowships at Harvard University, the Department of Astronomy at Harvard University, and the Department of Physics at Harvard University for their generous support of this project. We thank the anonymous referee for their comments.

Facilities: Tillinghast Reflector Echelle Spectrograph (TRES), Kepler Space Telescope (K2 Mission).

Software: Astropy (Astropy Collaboration et al. 2013, 2018, 2022), Radvel (Fulton et al. 2018).

Appendix A

RV Standard Stars Used for TRES Spectroscopy

As demonstrated by this paper, evolved stars in general and K giants like S364 in particular should be avoided when selecting RV standard stars. The instrumental zero-point for the S364 observations was monitored using three mid G to early K dwarfs: HD 38230, HD 65583, and HD 127334. The first and third stars had been well studied using the CfA Digital Speedometers and then HARPS-N, and they were shown to be constant over decades to the precision of those instruments. HD 65583 was chosen explicitly to serve as a standard for the CfA observations of M67, which date back forty years. Fortunately, it appears to be constant, too. All three have been followed with TRES from 2009 to the present. All three show an upward drift

of about $5 \text{ m s}^{-1} \text{ yr}^{-1}$ over the duration of the S364 observations, which we interpret as an instrumental drift. Table A1 presents the stellar parameters of the RV standard stars observed on the nights when S364 was observed.

A detailed review of the HD 65583 observations covering the period of S364 observations showed that for individual TRES runs, typically a month or more, the rms of the individual observations was less than about 20 m s^{-1} , and the standard deviation of the mean velocity was less than 5 m s^{-1} . The rms of the mean velocities, run-to-run in each year, was also less than 5 m s^{-1} , with a gradual shift of about 30 m s^{-1} between 2016 and 2022. This indicates that the run-to-run corrections of the instrumental zero-point are good at something like the 5 m s^{-1} level.

Table A1
RV Standard Stars for S364 Observations

Star	R.A. (2000)	Decl.	N_{obs}	T_{eff}^a (K)	$\log g^a$	T_{eff}^b (K)	$\log g^b$
HD 38230	05:46:01.9	+37:17:05	1663	5093	4.46	5237	4.52
HD 65583	08:00:32.1	+29:12:44	1432	5323	4.59	5238	4.56
HD 127334	14:29:36.8	+41:47:45	1339	5588	4.31	5671	4.27

Note. N_{obs} : the total number of TRES observations since 2009, T_{eff} : effective temperature, g : surface gravity (cgs). References: (a) Gaia DR3. (b) TIC 8.2.

Appendix B

Table of Radial Velocities for S364 from TRES








A portion of the relative radial velocities for S364 from TRES are reported in Table B1.

Table B1
Relative Radial Velocities for S364 from TRES (Abridged)

BJD	Relative RV (m s ⁻¹)	Error (m s ⁻¹)
2455615.859654	38.7	42.7
2456574.008505	-75.5	12.3
2457403.861292	-40.7	15.4
2457404.992365	-28.5	17.6
2457405.959878	-61.3	15.0
⋮	⋮	⋮
2459710.724881	-43.5	11.5
2459712.660429	-59.6	11.9
2459713.646983	-18.0	11.8
2459714.651510	-21.5	8.8
2459715.646913	-44.6	9.7

Note. The data is available on Zenodo under an open-source Creative Commons Attribution license: [10.5281/zenodo.7719269](https://doi.org/10.5281/zenodo.7719269). A portion is shown here for guidance regarding its form and content.

ORCID iDs

Qijia Zhou  <https://orcid.org/0000-0002-2028-8860>
 David W. Latham  <https://orcid.org/0000-0001-9911-7388>
 Samuel N. Quinn  <https://orcid.org/0000-0002-8964-8377>
 Allyson Bieryla  <https://orcid.org/0000-0001-6637-5401>
 Andrew Vanderburg  <https://orcid.org/0000-0001-7246-5438>
 Michael L. Calkins  <https://orcid.org/0000-0002-2830-5661>
 Gilbert A. Esquerdo  <https://orcid.org/0000-0002-9789-5474>

References

Akeson, R. L., Chen, X., Ciardi, D., et al. 2013, *PASP*, **125**, 989
 Astropy Collaboration, Price-Whelan, A. M., Lim, P. L., et al. 2022, *apj*, **935**, 167
 Astropy Collaboration, Price-Whelan, A. M., Sipőcz, B. M., et al. 2018, *AJ*, **156**, 123
 Astropy Collaboration, Robitaille, T. P., Tollerud, E. J., et al. 2013, *A&A*, **558**, A33
 Barnes, S. A. 2003, *ApJ*, **586**, 464

Brucalassi, A., Koppenhoefer, J., Saglia, R., et al. 2017, *A&A*, **603**, A85
 Brucalassi, A., Pasquini, L., Saglia, R., et al. 2014, *A&A*, **561**, L9
 Buchhave, L. A., Bakos, G. Á., Hartman, J. D., et al. 2010, *ApJ*, **720**, 1118
 Buchhave, L. A., Bizzarro, M., Latham, D. W., et al. 2014, *Natur*, **509**, 593
 Buchhave, L. A., Latham, D., Johansen, A., et al. 2012, *Natur*, **486**, 375
 Burke, C. J. 2008, *ApJ*, **679**, 1566
 Ceillier, T., Tayar, J., Mathur, S., et al. 2017, *A&A*, **605**, A111
 Choi, H.-J., Soon, W., Donahue, R. A., Baliunas, S. L., & Henry, G. W. 1995, *PASP*, **107**, 744
 Cumming, A., Butler, R. P., Marcy, G. W., et al. 2008, *PASP*, **120**, 531
 Dawson, R. I., & Fabrycky, D. C. 2010, *ApJ*, **722**, 937
 Döllinger, M. P., & Hartmann, M. 2021, *ApJS*, **256**, 10
 Döllinger, M. P., Hatzes, A. P., Pasquini, L., Guenther, E. W., & Hartmann, M. 2009, *A&A*, **505**, 1311
 Döllinger, M. P., Pasquini, L., Hatzes, A., et al. 2006, in Tenth Anniversary of 51 Peg-b: Status of and prospects for hot Jupiter Studies, ed. L. Arnold, F. Bouchy, & C. Moutou (Paris: Frontier Group), 138
 Dumusque, X., Boisse, I., & Santos, N. C. 2014, *ApJ*, **796**, 132
 Fűrész, G. 2008, PhD thesis, Univ. Szeged, Hungary
 Fulton, B. J., Petigura, E. A., Blunt, S., & Sinukoff, E. 2018, *PASP*, **130**, 044504
 Grunblatt, S. K., Huber, D., Gaidos, E., et al. 2019, *AJ*, **158**, 227
 Hatzes, A. P. 2013, *AN*, **334**, 616
 Hatzes, A. P., & Cochran, W. D. 1993, *ApJ*, **413**, 339
 Hatzes, A. P., & Cochran, W. D. 1996, *ApJ*, **468**, 391
 Hatzes, A. P., & Cochran, W. D. 1998, in ASP Conf. Ser. 154, Cool Stars, Stellar Systems, and the Sun, ed. R. A. Donahue & J. A. Bookbinder (San Francisco, CA: ASP), 311
 Hatzes, A. P., & Cochran, W. D. 1999, *MNRAS*, **304**, 109
 Hatzes, A. P., Cochran, W. D., Endl, M., et al. 2006, *A&A*, **457**, 335
 Hatzes, A. P., Cochran, W. D., Endl, M., et al. 2015, *A&A*, **580**, A31
 Hatzes, A. P., Endl, M., Cochran, W. D., et al. 2018, *AJ*, **155**, 120
 Howard, A. W., Marcy, G. W., Bryson, S. T., et al. 2012, *ApJS*, **201**, 15
 Howell, S. B., Sobek, C., Haas, M., et al. 2014, *PASP*, **126**, 398
 Kawaler, S. D. 1988, *ApJ*, **333**, 236
 Kurucz, R. L. 1992, in The Stellar Populations of Galaxies, ed. B. Barbuy & A. Renzini, Vol. 149 (Dordrecht: Kluwer), 225
 Mortier, A., & Collier Cameron, A. 2017, *A&A*, **601**, A110
 NASA Exoplanet Science Institute 2020, Planetary Systems Table, Last Accessed: 2022-07-22, IPAC, doi:[10.26133/NEA12](https://doi.org/10.26133/NEA12)
 Pietrinferni, A., Cassisi, S., Salaris, M., & Castellì, F. 2004, *ApJ*, **612**, 168
 Politis, D. N., & Romano, J. P. 1994, *Journal of the American Statistical Association*, **89**, 1303
 Reichert, K., Reffert, S., Stock, S., Trifonov, T., & Quirrenbach, A. 2019, *A&A*, **625**, A22
 Rein, H., & Liu, S. F. 2012, *A&A*, **537**, A128
 Rein, H., & Tamayo, D. 2015, *MNRAS*, **452**, 376
 Saio, H., Wood, P. R., Takayama, M., & Ita, Y. 2015, *MNRAS*, **452**, 3863
 Stassun, K. G., Oelkers, R. J., Paegert, M., et al. 2019, *AJ*, **158**, 138
 Stello, D., Vanderburg, A., Casagrande, L., et al. 2016, *ApJ*, **832**, 133
 Vanderburg, A., & Johnson, J. A. 2014, *PASP*, **126**, 948
 Vanderburg, A., Latham, D. W., Buchhave, L. A., et al. 2016, *ApJS*, **222**, 14
 Walker, G. A. H., Yang, S., Campbell, B., & Irwin, A. W. 1989, *ApJL*, **343**, L21
 Wisdom, J., & Holman, M. 1991, *AJ*, **102**, 1528